SCIENCE ROBOTICS | RESEARCH ARTICLE

MICROROBOTS

High energy density picoliter-scale zinc-air microbatteries for colloidal robotics

Ge Zhang[1]†, Sungyun Yang[1]†, Jing Fan Yang[1], David Gonzalez-Medrano[2], Marc Z. Miskin[2], Volodymyr B. Koman[1], Yuwen Zeng[1], Sylvia Xin Li[1], Matthias Kuehne[1], Albert Tianxiang Liu[3], Allan M. Brooks[1], Mahesh Kumar[1,4], Michael S. Strano[1]*

The recent interest in microscopic autonomous systems, including microrobots, colloidal state machines, and smart dust, has created a need for microscale energy storage and harvesting. However, macroscopic materials for energy storage have noted incompatibilities with microfabrication techniques, creating substantial challenges to realizing microscale energy systems. Here, we photolithographically patterned a microscale zinc/platinum/SU-8 system to generate the highest energy density microbattery at the picoliter (10^{-12} liter) scale. The device scavenges ambient or solution-dissolved oxygen for a zinc oxidation reaction, achieving an energy density ranging from 760 to 1070 watt-hours per liter at scales below 100 micrometers lateral and 2 micrometers thickness in size. The parallel nature of photolithography processes allows 10,000 devices per wafer to be released into solution as colloids with energy stored on board. Within a volume of only 2 picoliters each, these primary microbatteries can deliver open circuit voltages of 1.05 ± 0.12 volts, with total energies ranging from 5.5 ± 0.3 to 7.7 ± 1.0 microjoules and a maximum power near 2.7 nanowatts. We demonstrated that such systems can reliably power a micrometer-sized memristor circuit, providing access to nonvolatile memory. We also cycled power to drive the reversible bending of microscale bimorph actuators at 0.05 hertz for mechanical functions of colloidal robots. Additional capabilities, such as powering two distinct nanosensor types and a clock circuit, were also demonstrated. The high energy density, low volume, and simple configuration promise the mass fabrication and adoption of such picoliter zinc-air batteries for micrometer-scale, colloidal robotics with autonomous functions.

INTRODUCTION

The past decade has witnessed a surge of interest in scaling down sensors, robots, and computers to the submillimeter regime. For example, researchers have managed to shrink the volume of smart dust by nearly 1000-fold since its first proposal (*1*, *2*), yet the volume is still on the order of microliters (mm^3) (*3*–*6*). More recently, previously unknown materials and fabrication techniques have enabled even smaller sensors and machines invisible to the naked eye (*7*–*12*), with their lateral dimensions smaller than 100 μm and their volumes entering the picoliter (10^{-6} mm^3) regime. Such devices have been aerosolized (*10*), embedded into a polymer matrix (*8*), and injected into tissues (*8*). A notable recent achievement consists of picoliter robots that can walk using bimorph actuators as legs (*9*). However, energy storage has emerged as a limitation at the micrometer scale, which creates challenges in both material selection and fabrication (*13*). Conventional battery materials are prepared using wet chemistry that is fundamentally incompatible with the microelectronic fabrication processes used for these microrobotic advances (*14*), hence restricting most microbatteries to millimeters in size in the literature (*15*–*21*). Sub–square-millimeter batteries were only reported very recently, but they were neither picoliter sized nor colloidal (*22*–*24*). In this work, we photolithographically patterned high energy density microbatteries at the picoliter (10^{-12} liter) scale, demonstrating the capability to power robotic devices on the microscale.

A major motivation behind this trend of shrinking the size of robots is to unlock applications inaccessible to larger devices (*8*, *11*). A smaller size also enhances the mobility of sensors, enabling colloidal suspension of sensors and robots that can be carried along by fluid motion. To date, the majority of submillimeter-scale sensors were either powered by solar cells (*2*–*4*, *25*) or did not have internal power sources (*26*–*29*). However, to enable autonomous operation of colloidal robots in confined environments, such as pipelines, underground, in vivo, and on board, high energy density units are required given that access to ambient energy sources such as illumination is necessarily limited. Thus, there is a pressing need for integrating tiny batteries with tiny sensors and robots (*14*, *30*).

Our approach differs fundamentally from those used previously to create millimeter-sized batteries (*17*, *31*) because of the requirement for direct integration with microscopic loads through photolithography, which is challenging to achieve with postfabrication assembly methods (*14*, *32*). As mentioned above, conventional battery materials are prepared using wet chemical methods, such as slurry casting, that are fundamentally incompatible with microelectronic fabrication processes (*14*). This has apparently limited microbatteries to millimeters in size in the literature (*15*–*20*), which is 1,000,000 times larger in volume than the target load devices for emerging microrobotics (*32*–*34*). Similarly, the use of organic liquid electrolytes is another hurdle for fabrication, release (deployment), and biomedical applications (*35*–*40*). All-solid-state Li-ion batteries have been demonstrated with solid electrolytes (*41*–*44*), although the deposition of such ceramic materials is usually extremely slow (<0.01 nm s^{-1}). Nevertheless, the high air and moisture sensitivity of anode materials (such as Li metal or LiC_x) and

---

[1]Department of Chemical Engineering, Massachusetts Institute of Technology, Cambridge, MA 02139, USA. [2]Department of Electrical and Systems Engineering, University of Pennsylvania, Philadelphia, PA 19104, USA. [3]Department of Chemical Engineering, University of Michigan, Ann Arbor, MI 48109, USA. [4]Department of Electrical Engineering, Indian Institute of Technology, Jodhpur, 342030, India.
*Corresponding author. Email: strano@mit.edu
†These authors contributed equally to this work.

electrolytes complicates the fabrication processes, requiring hermetic sealing, which would inevitably expand the device volume for microrobotic applications (*38*, *39*). As a result, picoliter-sized full-cell Li-ion batteries that can be integrated with microscopic robotic components have not been demonstrated to date.

Zinc, as an anode material, has high stability under ambient conditions, which allows for a high deposition rate (>1 nm s^{-1}) and facile integration with standard photolithography processes. We selected Zn-air chemistry because theoretically it provides very high specific energy [1350 watt-hour (Wh) kg^{-1}] and energy density (>6000 Wh $liter^{-1}$) (*45*–*47*), which are essential metrics for microrobotic applications. Unlike other Zn-based batteries (*48*–*61*) in practice, primary Zn-air batteries also provide a high energy density of 1100 Wh $liter^{-1}$ (table S1) (*62*, *63*), much higher than that of rechargeable Li-ion batteries. We note that Zn is also compatible with physiological environments (*64*, *65*). Examples of Zn-air microbatteries in the literature to date (*62*, *63*, *66*–*72*) are millimeters in scale and are not suited for mass production or parallel release from a substrate, suggesting incompatibility with colloidal robotics.

In this work, we demonstrate a facile route for fabricating and subsequently releasing microscopic Zn-air batteries with cleanroom techniques in a massively parallel manner. Using dissolved oxygen, picoliter Zn-air batteries working in a neutral aqueous solution provided an energy density of more than 760 Wh $liter^{-1}$ (2.75 μJ pl^{-1}) and an areal power density of 0.15 mW cm^{-2}, with an open circuit voltage of 1.16 V. This represents the highest energy density for energy storage devices below 1 μl in volume. We found that because of the inherent high surface area–to–volume ratio, picoliter batteries do not require special materials or a sophisticated three-dimensional structure to achieve high energy density and power density. When the batteries operate in phosphate-buffered saline (PBS), commonly used to study physiological environments, the exposed Zn anode is shown to generate a zinc phosphate overcoating. This coating, however, does not impede the realization of high energy densities. We show that the batteries can switch on memristors and power actuators of similar sizes, demonstrating potential applicability to cell-sized autonomous robots. With linear dimensions ranging from 10 to 100 μm, the devices represent full-cell batteries capable of providing electricity to picoliter-sized machines.

RESULTS

Design, fabrication, and release of picoliter batteries

To scale Zn-air batteries down to the picoliter regime and to make them a modular component of microscopic machines, we designed a planar configuration as shown in Fig. 1, A to C. A typical device consisted of a 40 μm–by–50 μm Zn anode and a Pt cathode of the same size, both sitting on a 100 μm–by–100 μm polymer base (Fig. 1C). Smaller devices were also fabricated. Given that an aqueous ionic environment is typical for microrobotic applications, an electrolyte does not have to be incorporated during fabrication (Fig. 1A). This approach has been previously used on millimeter-scale devices and proven to be effective in simplifying the fabrication procedure (*68*, *71*, *73*, *74*). Harnessing both the cathodic material (O_2) and the electrolyte from the environment drastically improves the energy density, which is critical for reducing the size of colloidal robots. With standard photolithography, 10,000 batteries (a 100-by-100 array) of the same design can be fabricated on a single 2-inch (50.8-mm) wafer as shown in Fig. 1D. We verified that at least 98% of the electrode pads were intact after fabrication, with a resistance of less than 100 ohm (fig. S1A). By randomly sampling 134 devices across several wafers from different batches, we estimated the average open circuit voltage of the entire population to be 1.05 ± 0.02 V with a 95% confidence level (Fig. 1B), and we estimated the 95% confidence interval of the population SD to be 0.108 to 0.137 V. First, SU-8 polymer (2-μm thick) was cross-linked by contact photolithography to form a chemically stable, mechanically strong, and electrically insulating base (Fig. 1E) with a customizable thickness (fig. S2). Second, the platinum cathode was patterned and evaporated together with the current collector for the anode (Fig. 1F). From the bottom up, the Pt cathode consisted of a Ti (or Cr) adhesion layer, an Ag layer for mechanical flexibility, a second adhesion layer, and a functional layer of Pt. Last, the pattern for the Zn anode was defined, and a Ti adhesion layer was sputtered (Fig. 1G). Metallic Zn up to 1.5-μm thick (fig. S3) was deposited by thermal evaporation to complete the battery (Fig. 1H).

To enable facile release of microbatteries into solution, we fabricated them on a sacrificial substrate comprising a photoresist/Cu bilayer (Fig. 1A). After fabrication, a frame was patterned around each battery (Fig. 1I), where the Cu was etched away (fig. S4), and the photoresist was dissolved to release the batteries (Fig. 1J). The batteries can be stored in various solvents (Fig. 1K), such as tetrahydrofuran (THF) and acetonitrile, for more than 3 months. In addition to the open-circuit design in Fig. 1A, we also fabricated short-circuited designs where the Pt and Zn electrodes were connected (Fig. 1L and fig. S5). When the aged dispersion was transferred onto glass slides and dried, more than 90% of the batteries were observed to have an intact appearance (Fig. 1M). Almost all of them appeared flat, and the probability of the front side facing up was close to 50% (Fig. 1M and fig. S6). Short-circuited Zn-air batteries smaller than 50 μm were also produced, for which we adopted a design with Zn sitting at the center on top of the Pt (Fig. 1N). This configuration required lower fabrication accuracy and resolution, facilitating the down-scaling of device sizes. The 20-μm batteries can be released and remain intact after transferring onto slides (Fig. 1O), although the yield of release was much lower than that of the 100-μm devices (fig. S8). By measuring the number of Cu^{2+} ions displaced by Zn metal in a mixture of battery dispersion and copper(II) chloride solution (fig. S9), the thickness of Zn was verified to be consistent with that acquired by profilometry.

Performance of picoliter batteries

To characterize the electrical performance of these tiny batteries on a probe station, we fabricated some devices with extended leads (fig. S10). We connected one probe with each electrode through the leads to monitor the voltage and current of our batteries (fig. S10G). A drop of pH-neutral electrolyte solution was added to the device to emulate an operating environment for released picoliter batteries (*65*). The active device exposed to the electrolyte had the same design as the picoliter batteries in Fig. 1C, whereas the wires were covered by a layer of insulating SU-8 to prevent any interference with the measurements (fig. S10C). The amount of electrolyte was in large excess (~12.5 μl) compared with the device volume to minimize the effect of water evaporation. Batteries of various electrode sizes were fabricated on a sacrificial substrate so that they could undergo a release procedure similar to that experienced by batteries without wires (fig. S10, D to F).

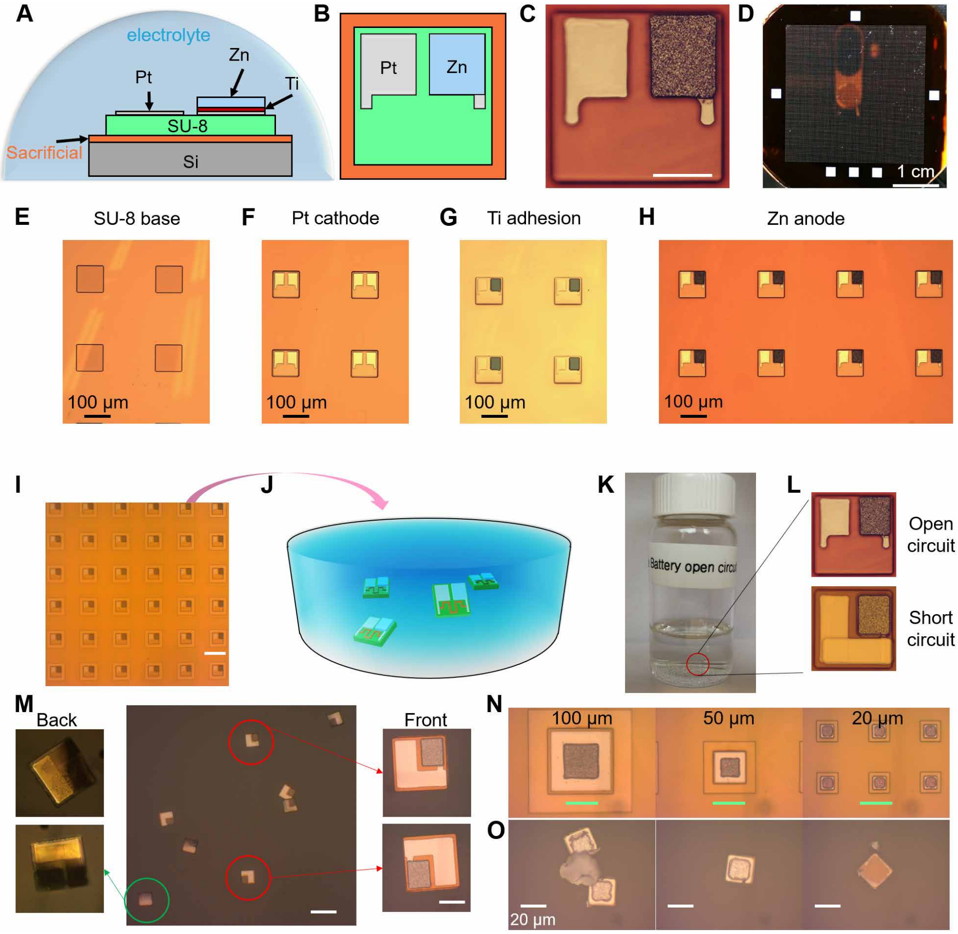

Fig. 1. Fabrication and release of Zn/Pt/SU8 picoliter Zn-air batteries. (**A**) Side-view schematic of a Zn-air picoliter battery placed in a droplet of electrolyte. (**B**) Height profile and (**C**) optical micrograph of an open-circuit Zn-air picoliter battery after fabrication. Scale bar, 40 µm. From (A) to (C), the SU-8 base has a side length of 100 µm. (**D**) Image of a Si wafer with a 100-by-100 array of picoliter batteries. (**E** to **H**) Optical micrographs of picoliter batteries at different stages of fabrication, as indicated by the annotation. (**I**) Optical micrograph of picoliter battery arrays patterned for Cu etching. Scale bar, 200 µm. (**J**) Schematics of batteries with loads (memristors in this case) released into solution. (**K**) Image of a bottle of dispersion containing 100-µm batteries. (**L**) Optical micrographs of open circuit and short-circuited Zn-air picoliter batteries; both are 100 µm. (**M**) Middle image: Optical micrographs of picoliter batteries deposited onto a glass slide. Scale bar, 200 µm. Side images: Optical micrographs of individual batteries that were facing down (left) and up (right). Scale bar, 50 µm. (**N**) Optical micrographs of short-circuited batteries of various sizes. Scale bars, 50 µm. (**O**) Optical micrographs of 20-µm batteries after releasing and redepositing onto a glass slide. The dust in the leftmost image was residual from the sacrificial substrate. The rightmost image shows a 20-µm battery that was facing downward. Scale bars, 20 µm.

Galvanostatic discharge of picoliter batteries was conducted in neutral electrolytes with 0.15 M of various salts (fig. S11). Batteries in PBS showed notably higher voltage and capacity compared with those in other electrolytes (Fig. 2A), despite a higher discharge rate. In PBS, identical picoliter Zn-air batteries were able to deliver more than twice as much energy and power as in other electrolytes (Fig. 2B). Meanwhile, the fluctuation of voltage in PBS was much more noticeable than that in any other solution (Fig. 2A). The PBS solution contained NaCl, KCl, KH_2PO_4, and Na_2HPO_4. Because neither control experiment with NaCl or KCl solution was able to replicate the performance in PBS, the phosphate buffer pair should be responsible for the superior energy and power. Inspection of the batteries after discharge revealed the existence of inorganic coatings on the Zn electrode in PBS, which was not observed in any other electrolyte (Fig. 2C and fig. S12). We identified the product as zinc phosphate formed by the following reactions in PBS, distinct from those for conventional Zn-air batteries, shown in Fig. 2D

$$\text{Cathode: } O_2 + 2\,H_2O + 4\,e^- \rightarrow 4\,OH^-$$

$$\text{Anode: } 3\,Zn + 6\,OH^- + 4\,H_2PO_4{}^- \rightarrow Zn_3\left(PO_4\right)_2 + 6\,H_2O + 2\,HPO_4{}^{2-} + 6\,e^-$$

$$\text{Overall: } 6\,Zn + 3\,O_2 + 8\,H_2PO_4{}^- \rightarrow 2\,Zn_3\left(PO_4\right)_2 + 6\,H_2O + 4\,HPO_4{}^{2-}$$

On the cathode, Pt catalyzes the reduction of oxygen to form hydroxide ions, which is the same as in Zn-air batteries with the other tested electrolytes. On the anode side, instead of reacting with water to form zinc hydroxide, Zn^{2+} reacts with phosphate ions ($PO_4{}^{3-}$) to form a precipitate, and the hydroxide ion from the cathode is buffered by $H_2PO_4{}^-$. This mechanism is consistent with previous reports on macroscopic Zn-air batteries using a similar electrolyte (*75*).

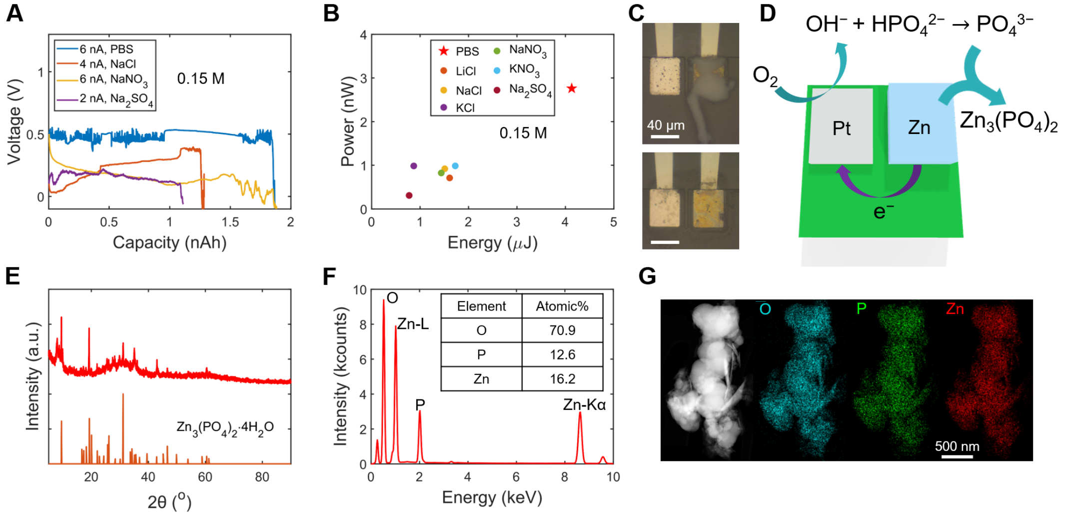

Element	Atomic%
O	70.9
P	12.6
Zn	16.2

Fig. 2. Reaction mechanism in picoliter Zn-air batteries. (**A**) Galvanostatic discharge curves of picoliter Zn-air batteries in several representative electrolytes. (**B**) Power versus energy plot (Ragone plot) extracted from galvanostatic discharge of picoliter batteries in various electrolytes. The concentration of cations was 0.15 mol/liter in all electrolytes except PBS. The current of discharge was the highest possible value for the voltage to be positive in each electrolyte, which was 2 nA in sodium sulfate, 4 nA in lithium/sodium/potassium chloride, and 6 nA in sodium/potassium nitrate and PBS. (**C**) Optical micrographs of picoliter batteries after galvanostatic discharge in PBS (top) and LiCl (bottom). Scale bars, 40 μm. (**D**) Schematics of the half reactions and the overall reaction. (**E**) XRD spectrum of the discharge product and the reference spectrum of hydrated zinc phosphate (hopeite). a.u., arbitrary units. (**F**) EDS spectrum of the discharge product in PBS solution, with atomic percentage of the major elements, acquired with a STEM. (**G**) HAADF image and EDS mapping of the discharge product in the same region where the EDS spectrum was collected.

The reaction mechanism above was confirmed by energy dispersive x-ray spectroscopy (EDS) and x-ray powder diffraction (XRD) characterization of the discharge product in PBS. Most peaks in the XRD spectrum were assigned to zinc phosphate tetrahydrate (Fig. 2E). Quantitative analysis of the EDS spectra revealed a Zn:P:O atomic ratio of about 3:2.3:13 (Fig. 2F), consistent with the chemical composition determined by XRD. The EDS mapping showed a uniform distribution of Zn, O, and P across the particles (Fig. 2G), suggesting a homogeneous composition. The discharge product is likely a mixture of amorphous and crystalline components, given that e-beam diffraction showed no discernible structure for most regions probed, whereas the XRD results demonstrated crystallinity. On the basis of this evidence for a $Zn_3(PO_4)_2$ layer, our observed voltage fluctuations were attributed to stochastic pitting corrosion of the Zn anode (*76*, *77*). In PBS, $Zn_3(PO_4)_2$ precipitated at a lower Zn^{2+} concentration than $Zn(OH)_2$ [Fig. 2, E to G, and Supplementary Discussion (the "Dissolution equilibrium and electrode potential in PBS solution" section)], which is the main precipitate in the other neutral electrolytes tested. As a result, a thicker, more continuous, and less permeable passivation layer formed on Zn during galvanostatic discharge in the PBS electrolyte, leading to more marked voltage fluctuations when pitting corrosion occurred. The mechanical disturbance generated by the growing zinc phosphate film may also have contributed to the voltage fluctuations. We also noted that the voltage fluctuations of our battery were larger than those in the literature because of the smaller size and the lack of an ion-exchange polymer coating (*75*). A picoliter battery is expected to have a larger fluctuation than a macroscopic one, because the inhomogeneity of the electrode material plays a larger role on a smaller area. However, the higher overall power and energy density we observed in PBS compared with those in other electrolytes indicate that this passivation layer reduces the self-discharge of the Zn anode (*75*). Ideally, a passivation layer (or solid electrolyte interphase) for a Zn anode should be continuous, uniform, nonporous, conductive to Zn^{2+}, and mechanically strong. In our case, although the zinc phosphate precipitate (hopeite) was conductive to Zn^{2+}, it was not uniform and continuous. To improve the uniformity of the zinc phosphate passivation layer, a layer of Nafion coating can be applied given that it has been shown to be effective in the literature (*75*). The fluctuation in the first 2000 s of discharge was typically less than 100 mV, which is about 10% of the open-circuit voltage (OCV). We demonstrated that the battery can provide reliable power to many types of microrobotic loads.

Encouraged by the exceptional performance, we further studied these picoliter Zn-air batteries in the PBS electrolyte. Voltage curves were measured by discharging the batteries at increasing current densities (per cathode area) from 0 to 0.75 mA cm^{-2}. Data were collected from nine individual batteries (Fig. 3A) and averaged. The voltage monitored over 60 s at each current density is shown in Fig. 3C, and the time-averaged voltage versus current curves (polarization curves) were obtained as shown in Fig. 3B. The OCV of these batteries was around 1.2 V, and the short circuit current was about 10 nA (0.5 mA cm^{-2}). When we plotted the average voltage versus the normalized current (Fig. 3B and fig. S13), we found that the polarization curves were mostly invariant with respect to size. This indicates that the cell resistance scales with the size of the electrode and that the oxygen transport on the cathodic side is likely the rate-determining step. This is further supported by literature results that the discharge current scaled linearly with the cathode area when the Zn area was fixed (*78*). This is also consistent with a much higher current density of oxygen reduction reaction when the catalyst was loaded on a rotating ring-disk electrode (*79*, *80*) or at the triple phase boundary (*45*–*47*), where the transport of oxygen was greatly enhanced compared with our setup. We therefore normalized the current and power on the basis of the cathode area.

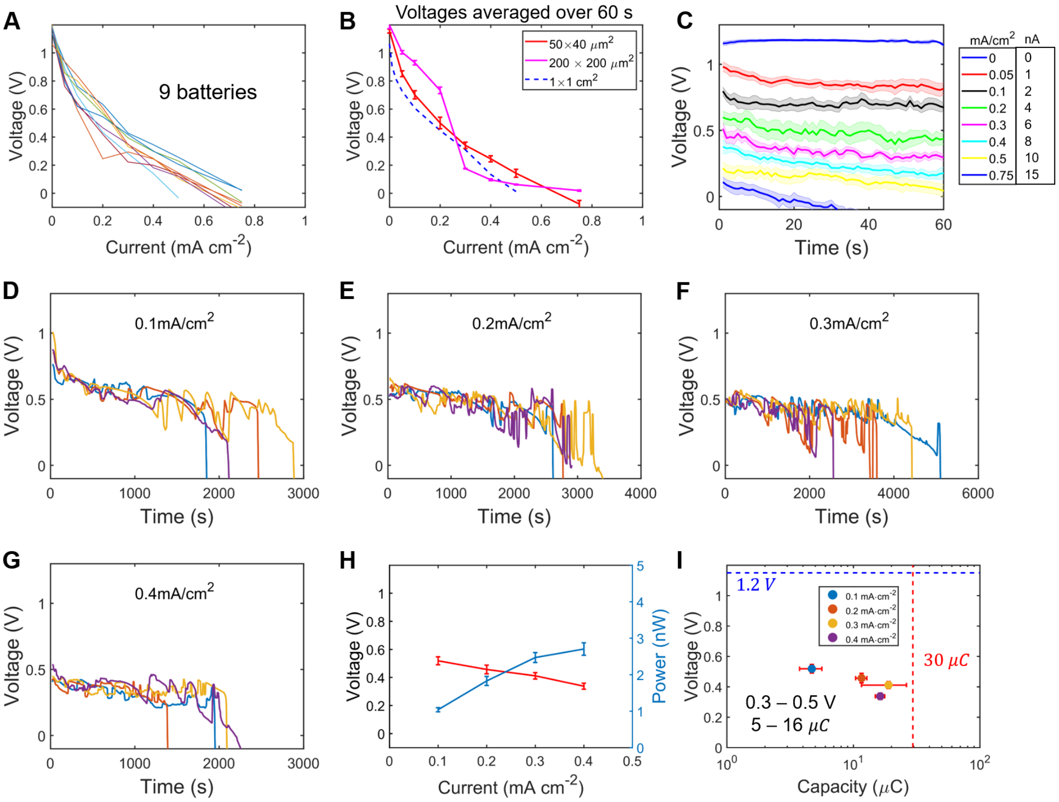

Fig. 3. Performance of picoliter Zn-air batteries in PBS. (**A**) Polarization curves of nine individual batteries with 50 μm–by–40 μm electrodes. (**B**) Polarization curves from batteries of three different electrode areas. (**C**) Voltage versus time curves for Zn-air picoliter batteries under different discharge current densities; the shaded regions indicate the SE of the measurement. The legend shows the correspondence between the actual current and current density normalized by the area of the Pt electrode. (**D** to **G**) Galvanostatic discharge curves of picoliter Zn-air batteries under current densities of (D) 0.1 mA cm^{-2}, (E) 0.2 mA cm^{-2}, (F) 0.3 mA cm^{-2}, and (G) 0.4 mA cm^{-2}. Data from four devices are shown for each rate; more discharge curves can be found in figs. S13 and S16. These batteries have 1-μm-thick Zn and a volume of 2 pl. (**H**) Polarization curve and power curve generated by averaging the galvanostatic discharge curves in (D) to (G). (**I**) Average voltages and capacities of batteries under four current densities. The theoretical capacity and open circuit voltage are indicated by the dashed lines.

Figure 3, D to G, shows the long-time galvanostatic discharge data of the picoliter batteries in PBS with various current densities. The thickness of Zn was supposed to be 700 nm on the basis of the quartz balance in the deposition chamber, whereas the actual thickness measured by the profilometer was 1 μm, likely because of the loose packing of Zn microcrystals. The average voltage dropped from about 0.5 V (Fig. 3D) to 0.3 V (Fig. 3G), whereas the average output power increased from 1 nW to near 3 nW (Fig. 3H) as the discharge rate increased from 0.1 mA cm^{-2} (0.24 C) to 0.4 mA cm^{-2} (0.96 C). This trend (Fig. 3H) was consistent with the voltage-current relationship obtained in the previous experiment (Fig. 3B). The fluctuating voltage observed in Fig. 2A was also seen here under various discharge rates. The duration of discharge did not decrease accordingly but stayed roughly around 2000 to 3000 s (Fig. 3, D, E, and G), with an exception at 0.3 mA cm^{-2} (Fig. 3F). This corresponds to an increase in capacity from one-sixth to more than 50% of the theoretical value (30 μC) as the discharge accelerated (Fig. 3I), which is opposite to the common trend in most batteries. Self-discharge may explain the limited operation time of the Zn anode, leading to a lower capacity at lower discharge rates. The discharge product growing on the surface of the Zn anode could eventually block its access to the electrolyte, which might also lead to a premature failure (fig. S14). However, some exceptions do exist at high rates (above 0.3 mA cm^{-2}) with close-to-theoretical capacity (blue curve in Fig. 3F and yellow curve in fig. S15D), which did not exhibit self-discharge for a much longer time (>4000 s). The released batteries with wires delivered one-third less capacity compared with batteries tested on wafer (fig. S16) because of damages to the Zn electrode during the release and transfer process, which involved a series of mechanical manipulations and repeated solvent washing. Aging of the batteries in the solvent for more than 1 month does not appear to lead to failure of the picoliter batteries (fig. S15, E and F).

A Ragone plot of the individual performance of each tested battery shows reasonable consistency across devices under the same testing condition (Fig. 4A). Unlike the commonly observed negative correlation between energy and power densities (red squares in Fig. 4B), there appeared to be a somewhat positive correlation for our picoliter Zn-air batteries. This is because of the self-discharge effect discussed in the previous paragraph. Because the cathodic reactant O_2 came from the solution environment, the net volume of the battery (2 pl) was dominated by the Zn anode, whereas the Pt cathode accounted for less than 10% of the volume. The total output energy of one picoliter battery was about 5.5 μJ at 0.4 mA cm^{-2}, which translates to an energy density of 2.75 μJ pl^{-1} (~760 Wh liter^{-1}). At 0.3 mA cm^{-2}, devices with exceptionally high energy densities (near 6 μJ pl^{-1}) gave rise to a higher average of 3.85 μJ pl^{-1}

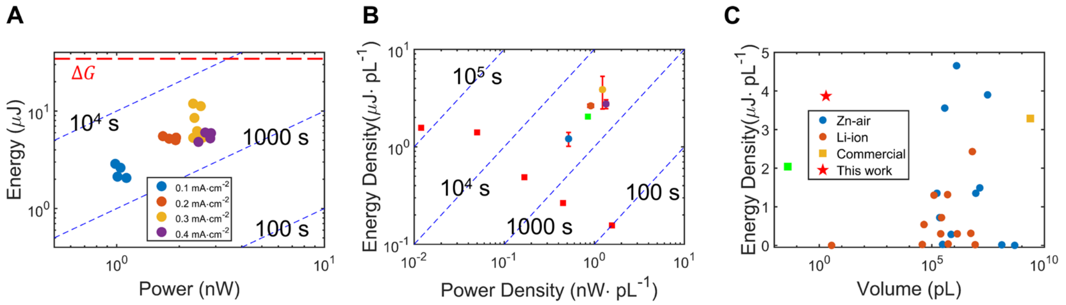

Fig. 4. Performance summary and comparison. (**A**) Ragone plot of energy and power of individual batteries with a 2-pl volume; the data were calculated from Fig. 3, D to G. The theoretical Gibbs free energy of the cell reaction is shown as the red dashed line. (**B**) Ragone plot of the average energy and power densities under four current densities. The error bars represent the SD across multiple devices. The red squares are data of Li-MnO_2 primary microbatteries from the literature (*89*). The green square is a data point of Al (aluminum)–H_2O microbattery from the literature (*90*). (**C**) Master plot of the energy density versus cell volume for various microbatteries reported in the literature (electrolyte volume excluded for all entries). This work is shown with a red star.

(1070 Wh liter^{-1}). Compared with Li-ion microbatteries reported in the literature (*15*–*18*, *31*, *38*, *43*, *44*, *81*–*83*), our Zn-air battery benefits from harvesting part of its reactants from the environment and hence offers a higher energy density, among other advantages (Fig. 4C), despite its simple structure and facile fabrication. It has a volume five orders of magnitude smaller than almost all microbatteries in the literature. Therefore, we demonstrated the releasable picoliter-sized battery that has appreciable energy density and can be fabricated with standard photolithography, which makes it a promising energy source for cell-sized robots and sensors (*8*–*10*).

Powering microrobotic loads

Memristors are two-terminal devices whose resistance is modulated on the basis of the history of current passing through. We used memristors in the past for information storage on a colloidal state machine with a relatively simple structure (*10*, *11*). In this work, commercial memristors purchased from Knowm Inc. were connected with picoliter batteries in a setup shown in fig. S25A. The cyclic voltammetry curves of the memristors (fig. S25C) show that they can be switched from an off state with 1 gigohm resistance to an on state with 1 to 10 megohm resistance at a threshold voltage of around 0.2 V, making them suitable loads for our picoliter batteries. Figure 5A shows that after 20 min of discharging, a memristor can be successfully turned on by a Zn-air battery with only a 2-pl volume. Compared with the control devices that remained in the off state, devices that were connected to the batteries exhibited a substantial increase in conductance of up to three orders of magnitude (Fig. 5B). The relatively large variation in the final on-state conductance was attributed to variabilities in both the batteries (Fig. 3) and the memristors (fig. S25) and was likely magnified by the nonlinear switching characteristic of the memristors. Nevertheless, all devices showed on-off ratios larger than 3, which was a marked change in the current-voltage (*I*-*V*) curves (fig. S26). In comparison, the control samples had almost no increase in the conductance (on-off ratios less than 1.5). This experiment confirmed the capability of picoliter batteries to power microscopic electronic devices. The memristors had a length scale of around 50 μm and hence could potentially be integrated with our batteries to enable the construction of fully autonomous colloidal robots (*84*).

Recently, Miskin *et al.* (*9*) demonstrated Pt-Ti bilayer metallic actuators as legs for microscopic robots. Bias voltages applied on the actuator caused the adsorption/desorption of hydrogen or oxygen species on the Pt surface (*9*), which changed the stress distribution and the curvature of the device (Fig. 5C). Once connected with the Zn electrode of the battery, the actuator bent from its flat state (50-μm long, 12-μm wide) to a maximum curvature of around 0.1 μm^{-1} in about 4 s (Fig. 5, D and E, and movie S1). When we reversed the bias by connecting the Pt cathode of the battery with the actuator, it relaxed to the flat state at a similar rate. The response time is in agreement with the RC time constant of the circuit (Supplementary Methods). We showed that another 60 μm–by–14 μm actuator could be powered by a 1.6-pl battery to quasireversibly bend and flatten for more than 50 cycles (fig. S27 and movie S2). After prolonged operation, a decay in the minimum curvature (maximum actuator length) was observed (Fig. 5, D and E, and fig. S27, B and C), accompanied by a slowing down of the flattening response time to more than 10 s. Meanwhile, the maximum curvature and the curling response time remained almost unchanged. This was possibly because of some irreversible changes in the actuator during repeated actuation under high voltage (*85*) as evidenced by the difficulty flattening it afterward (fig. S28 and movie S3). The total current passing through the actuator consisted of a pulse component from capacitive discharge and a constant part from Faradaic current, as shown in Fig. 5F. It is estimated that about 60% of the battery's total energy was consumed by the actuator (Supplementary Methods), mostly to drive the Faradaic reactions. The disparity between the positive and negative Faradaic currents is explained by a difference in the reduction and oxidation reaction rates on the actuator.

Sensors are essential components for the autonomous operation of a microrobot; hence, we further demonstrated the capability of our picoliter battery by powering resistive chemical sensors. In Fig. 6, A and B, two chemical sensors made of different materials were both successfully powered by picoliter batteries. When a water droplet containing the analyte triethylamine (TEA) was added onto the monolayer MoS_2 sensor, the impedance of the device decreased, and thus the output current of the battery increased significantly (Fig. 6A) (*10*). The other sensor based on a single-walled carbon nanotube (SWNT) was less sensitive than the MoS_2 sensor, requiring a higher analyte concentration and rendering a smaller signal but still producing a marked change in the output current (Fig. 6B). Note that neither device was optimized for this application. Nevertheless, their responses (ΔI ~ 20 nA) were large enough to drive at

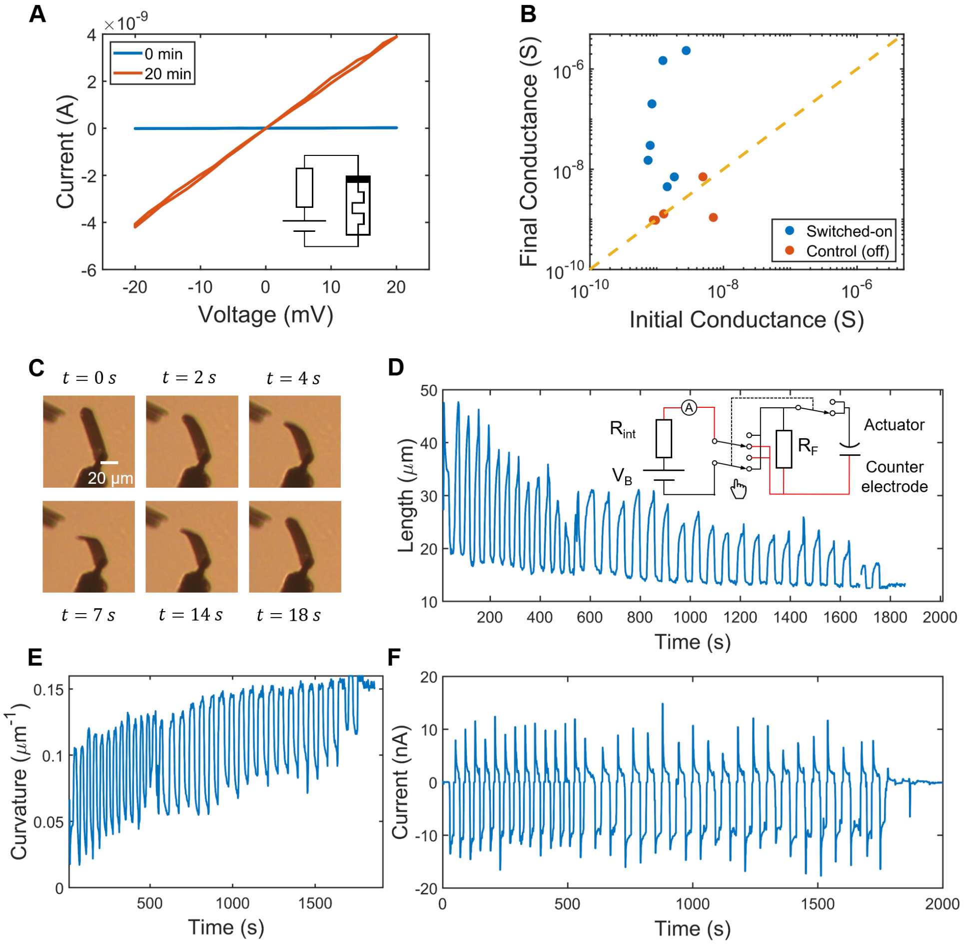

Fig. 5. Application of Zn-air batteries. (**A**) *I-V* curves of a memristor connected with a 100-μm picoliter battery (2 pl) before and after 20 min of discharging in the PBS electrolyte. The batteries are from the same batch of devices used for performance characterization in Fig. 3. The inset shows the schematic of the circuit. *I-V* curves of other switched-on devices can be found in fig. S26. (**B**) Scatterplot of the initial and final conductance of memristor devices that were switched on by batteries (blue) versus those not powered (orange). (**C**) Images of a Pt-Ti surface electrochemical actuator (SEA) curling and flattening under cyclic voltammetry measurement with 0.4-V amplitude. A Pt wire was used as the counter electrode. The curvature of the actuator increased when sweeping toward negative bias and decreased when sweeping toward positive (fig. S28). (**D**) Length of a 50 μm–by–12 μm SEA over 35 cycles of actuation powered by a 1.6-pl battery. The battery was in a separate solution from the SEA. The inset shows the circuit diagram used in this experiment. (**E**) Curvature of the actuator during operation converted from the length shown in (D). (**F**) Current recorded by an ammeter during the actuation shown in (D).

least some potential loads, such as the aforementioned memristors and actuators. The very large current means that the on-state resistance of the MoS_2 sensor is negligible compared with the internal resistance of the battery or the resistance of a bimorph actuator. Therefore, if an actuator and a sensor are connected in series, a battery is essentially directly powering the actuator when the sensors are turned on. If paired with memory devices, then our batteries could provide the energy necessary to record environmental information as nonvolatile memory in the form of resistance change to be recovered later.

Last, our batteries also enabled a basic and key function for all autonomous machines, which is a clock signal generator. Using a simple relaxation oscillator (Fig. 6C) composed of a picoliter battery, a resistor (1 gigohm), a capacitor (4.7 nF), and two commercial complementary metal-oxide semiconductor inverters (SN74HC04), we managed to generate a regular AC signal. The amplitude of the signal had some variation over time because of the voltage fluctuation of the battery, but a stable frequency of 0.1 Hz was maintained over the entire discharge period (Fig. 6D). Such a stable, low-frequency clock signal would enable the microrobot to keep track of time and perform sequential logic operations (*86*). A more efficient oscillator design and much more complex microchiplet circuits have already been demonstrated in the literature (table S2), most of which require power on the order of nanowatts when in standby mode (not performing data transmission). Overall, we demonstrated the ability of the picoliter batteries to drive five different applications, including a memristor, an actuator, two types of sensors, and one oscillator circuit.

Proof-of-concept experiments

Although our colloidal batteries are intended to operate in a large reservoir of electrolyte, there are other application scenarios where the microrobots are in a dry environment or where ionic species are not available in the liquid environment. To this end, we carried out

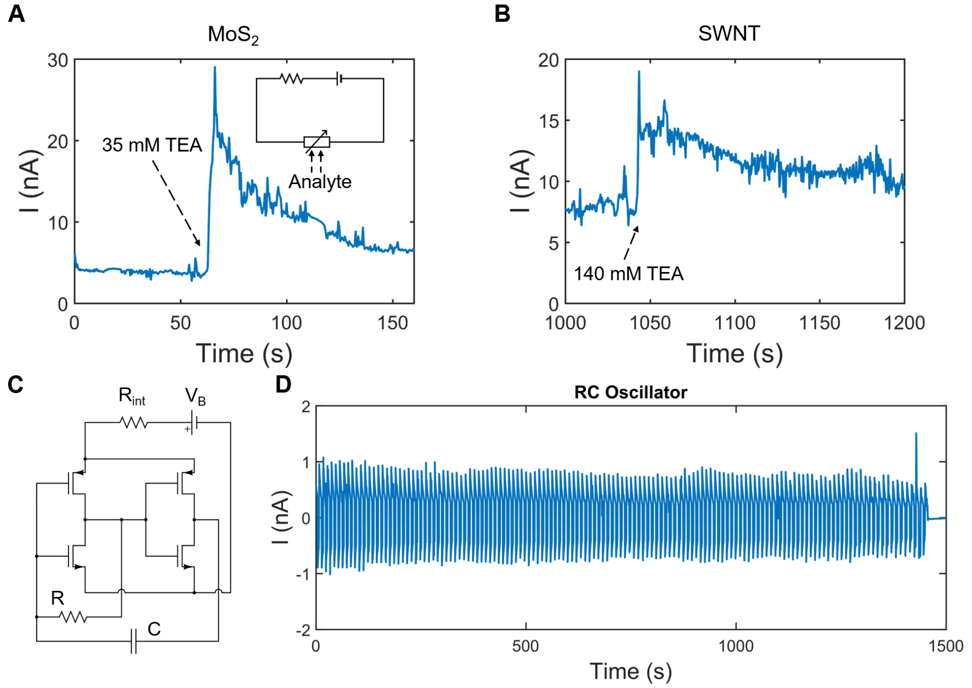

Fig. 6. Application of Zn-air batteries continued. (**A**) *I-V* curves of an MoS$_2$ chemiresistor connected with a picoliter battery (2 pl) during the addition of a droplet containing 35 mM TEA. (**B**) *I-V* curves of a SWNT chemiresistor connected with a picoliter battery (2 pl) during the addition of a droplet containing 140 mM TEA. (**C**) Circuit diagram of an RC oscillator with two inverters powered by a picoliter battery. (**D**) Current signal of the RC oscillator over 1500 s.

two proof-of-concept experiments demonstrating the potential of picoliter Zn-air batteries. For the first scenario, where a closed battery is preferred, we used a micro–inkjet printer to precisely drop 500 pl of ionic liquid (IL) electrolyte onto our batteries (Fig. 7A). The batteries offered lower voltage compared with those in the normal PBS electrolyte, primarily because of the higher viscosity and lower conductivity of IL electrolyte. The battery delivered 0.82 μJ of energy at a current density of 0.1 mA cm^{-2}. Although smaller than PBS-based batteries, the batteries with IL still delivered energy density (1.6 nJ pl^{-1}; electrolyte volume included), still outperforming the smallest energy storage devices in the literature (*22*). Further reduction of electrolyte volume and introduction of a box to seal the IL could allow for a self-contained picoliter-sized battery. In the second experiment, we added 20 pl of salt to the battery by drying a dilute electrolyte solution. When immersed in a droplet of deionized (DI) water (about 10 μl), the battery released salt and was able to deliver 0.6 to 1.2 μJ of energy at a current density of 0.1 mA cm^{-2} (Fig. 7B). The very low concentration of salt results in low conductivity and a reduced discharge potential, similar to the case of using IL electrolyte. This semiclosed, salt-releasing configuration ensures that the picoliter batteries can operate even without ions in the environment. Overall, these experiments show that the Zn-air batteries could potentially operate in different environments and do not necessarily require an infinite electrolyte reservoir.

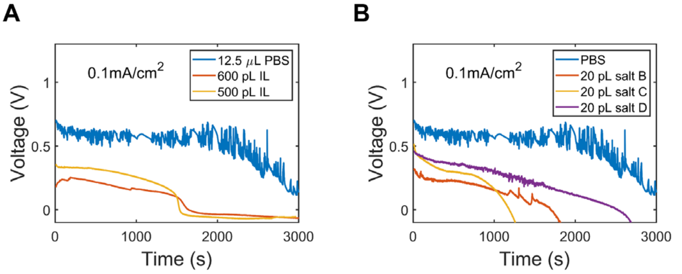

Fig. 7. Alternative picoliter Zn-air battery designs for various application scenarios. (**A**) IL-based batteries for applications that require a closed-battery configuration. Galvanostatic discharge curves of Zn-air batteries in 500 to 600 pl of IL under a current density of 0.1 mA cm^{-2}. The IL electrolyte is composed of 1 M Zn(BF$_4$)$_2$ in 1-ethyl-3-methylimidazolium tetrafluoroborate [(EMIM)(BF$_4$)]. (**B**) Semiclosed, salt-releasing batteries for applications in pure water. Galvanostatic discharge curves of Zn-air batteries carrying 20 pl of salt, under a current density of 0.1 mA cm^{-2}. The salt-carrying batteries were immersed in 10 μl of DI water.

DISCUSSION

Compared with other microbatteries reported to date, the Zn-air picoliter batteries reported in this work offer one of the highest energy densities (Fig. 4C), but their power density has substantial room for improvement (fig. S29). We note that increasing the power density is helpful for performing tasks like locomotion and communication (table S2). Building on these capabilities, in the future, we plan to explore the possibilities of creating autonomous cell-sized robots capable of self-powered sensing, steering, and locomotion. Improvements will therefore enable substantial increases in capability and task flexibility for microscopic sensors and robots. We identified the cathodic reaction, or more accurately the transport of O$_2$, as the rate-limiting step in this system. Hence, the easiest next improvement is to increase the area of the Pt cathode. However, the size of Pt is constrained by the projected area of the device to be powered, whereas increasing the specific area is ineffective. Alternatively, we may increase the access to oxygen by creating triple phase boundaries, which may require a polymer/gel electrolyte compatible with photolithography. Replacing the Pt with other types of cathode, such as Ag_2O, MnO_2, and NiOOH, may remove the limitation of O_2 in solution (fig. S30, A to C). To mitigate the large voltage fluctuation toward the end of discharge, a larger discharge rate or a conformal polymer coating on Zn may also be desirable (fig. S30, D to F). In future work, we plan to explore Zn-based picoliter batteries with a higher power density and rechargeability.

It is worth mentioning that because many of our targeted loads, such as the bimorph actuator and the sensors, need to work in an aqueous environment, the integration of a picoliter Zn-air battery with those loads is expected to be easy and natural. Other loads that might be sensitive to liquid, such as some microelectronic circuits, need to be encapsulated anyway for the colloidal robots to work in solution. Therefore, the integration of a battery with those encapsulated loads will not be a problem either.

The primary battery demonstrated in this study is suitable for some application scenarios that we have envisioned (*84*). However, other applications such as implantable microelectronics may call for a rechargeable battery. The nonevaporating IL electrolyte and the air-independent Ag_2O cathode pave the way toward fully enclosed battery systems, which are much easier to recharge than an open cell. Enclosed batteries can also be connected in series to provide higher voltage. In a rechargeable battery, the depth of discharge may need to be limited to prevent Zn delamination, therefore sacrificing some energy density. Substantial engineering and optimization are needed to make Zn-air picoliter batteries with cycle life, energy, and power density comparable to those of their macroscopic counterparts (hundreds of cycles and up to 2000 Wh liter^{-1}) (*87*). It is also preferable to embed picoliter batteries as a structural part of microrobots, as demonstrated in macroscopic robots as well (*87*, *88*).

In summary, we present the fabrication, release, characterization, and application of Zn-air picoliter batteries. Using standard photolithography, we fabricated thousands of picoliter batteries on a single wafer at once that were easily released into solutions. Batteries of various sizes were created, ranging from 10 to 100 μm across. The electrochemical performance of these batteries was characterized on a probe station by galvanostatic discharge. The performance achieved was in agreement with our expectation, with an open circuit voltage of 1.2 V, a short circuit current density of about 0.5 mA cm^{-2} (10 nA/2000 μm^2), a power of 0.15 mW cm^{-2} (3 nW/2000 μm^2), and a capacity of 300 mAh g^{-1} (16 μC/2 pl). Our picoliter batteries demonstrated an energy density of up to 1070 Wh liter^{-1}, exceeding those of most microbatteries to date. Last, the tiny batteries were proven to be able to turn on memristors and drive actuators of comparable sizes. The high energy density, compatibility with photolithography, and relatively simple fabrication process make picoliter Zn-air batteries a desirable power source for colloidal electronics. This work may inspire more effort toward picoliter-scale energy storage and harvesting devices and greatly expand the functionality and application of cell-sized robots and sensors.

MATERIALS AND METHODS

Picoliter battery fabrication

A layer of LOR-3A lift-off resist was first spin-coated onto a 2-inch (50.8-mm) Si wafer at 2000 rpm. The coated wafer was then baked at 180°C for 4 min and 190°C for 20 min to increase the stability of LOR-3A during fabrication. A layer of 70-nm-thick copper was subsequently deposited on top of the LOR-3A by DC magnetron sputtering (AJA International). This formed the sacrificial LOR/Cu substrate, enabling easy release of batteries in later experiments. During fabrication, the Cu layer protects the photoresist from being dissolved in the lift-off solution (Remover-PG).

To define an insulating base for the batteries, we first patterned SU-8 2002 negative photoresist by contact photolithography on an MA-6 mask aligner. After development, the cross-linked SU-8 structure was hard-baked at 120°C for 4 min to increase adhesion and reduce stress. In the second photolithography step, LOR-20B and Shipley S1805 photoresist were patterned to define the electrical contacts to both electrodes. Wafers with only 100-μm batteries were patterned by contact photolithography, whereas wafers with various sizes of batteries were patterned by direct laser writing in a maskless aligner (Heidelberg MLA-150). A tri-layer metal of 5 nm/20 nm/5 nm Cr/Ag/Cr (or Ti/Ag/Ti) was deposited by a Denton electron-beam evaporator, followed by 25 nm of Pt deposited by either e-beam evaporation or DC sputtering. The lift-off process was performed in Remover-PG solution on a shaker to remove the photoresist and extra metal. The third step used the same photoresist as the second step to define the Zn anode pattern. A titanium adhesion layer (10 nm) was first sputtered, after which Zn metal was deposited by a Key High thermal evaporator. The thickness of Zn was monitored with a quartz crystal oscillator in the evaporation chamber. The lift-off process was performed in Remover-PG on a shaker at room temperature. For Zn-Ag_2O batteries, the cathode material was deposited by reactive sputtering of Ag target in O_2/Ar plasma. Last, Shipley S1818 was coated and patterned to protect Zn and define an etching frame around each battery.

The fabrication of batteries with wires for electrical characterization shared the same procedure as described above, except for an additional step before the last one. Another layer of SU-8 2002 was patterned after finishing the third step to shield the wires from electrolyte while exposing the active region of the device. Some of the batteries with wires were fabricated on another insulating substrate, such as SiO_2 or glass, and were tested without releasing.

Release procedure

The as-fabricated wafer was immersed in Cu etchant 49-1 for 2 min to remove Cu in the etching zone around each battery. The wafer was then washed with DI water and acetone to dissolve the S1818 photoresist. Subsequently, the wafer was immersed in 20 ml of THF for 3 to 4 hours to dissolve the LOR sacrificial layer. After releasing most of the batteries, the wafer was taken out, and THF was evaporated to less than 5 ml. Optionally, the photoresist-containing solution was then diluted by adding fresh solvent (THF or acetonitrile) and taking out old solvent with a pipette. The resulting dispersion was then collected for future characterization.

The yield of the fabrication process was more than 95% (less than 1 device per 200 was observed to be defective under microscope). The yield of the release procedure was about 90% (roughly 10% of batteries were stuck on the wafer and were not released). The released batteries were mostly intact (95% of the upward-facing batteries looked visually the same as they did before releasing). All of the released batteries could be discharged (even the ones that were facing downward). Overall, we estimate an overall yield of at least 80% for the functional picoliter batteries after being released from the substrate.

The batteries with wires were also etched and washed in the same way as stated above. Then, 2 μl of poly(methyl methacrylate) (PMMA) e-beam resist was drop-casted onto each device as a protection layer. After drying and annealing, the wafer was immersed into 2 wt % KOH solution to release the devices. The floating devices after releasing were fished with glass slides and cleaned with DI water and acetone.

Characterization

Optical images of batteries were acquired with a Zeiss Axio Scope A1 microscope using objective lenses of various magnifications (5×, 10×, 50×, and 100×). The height profiles of the batteries were measured with a Bruker DektakXT profilometer using a 2-μm-radius diamond-tipped stylus. The ultraviolet-visible spectra of batteries in copper chloride solution were measured with a Shimadzu UV-3101PC spectrophotometer at wavelengths of 250 to 600 nm. The discharge product was collected from a macroscopic Zn-air cell in PBS solution, centrifuged and washed twice with DI water, and dried for further characterization. The dried powder was dispersed in isopropanol and loaded onto a transmission electron microscopy grid for high-angle annular dark-field (HAADF) and EDS mapping on a Titan Themis Z G3 Cs-corrected scanning transmission electron microscope (STEM). The powder XRD was measured with a PANalytical X'Pert Pro diffractometer.

Electrical characterization

Electrical performance measurements of picoliter batteries were performed on an ARS PSF-10-1-4 Cryogenic Probe Station using micromanipulators as probes. All measurements were done on batteries with wires in a two-electrode configuration under ambient conditions. One probe connected to the Pt electrode served as the working electrode, and the other probe connected to the Zn electrode served as the counter and reference electrode. Voltage and current were applied to the probes using a semiconductor parameter analyzer (Agilent E5262A source measure units, controlled by MATLAB code). Before measurement, a drop of PBS or one of the other types of electrolytes (10 to 15 μl) was added to the active region of the device. The droplet did not spread out to the probes because of a large contact angle with the SU-8 polymer. Voltage polarization curves were obtained by sequentially increasing the galvanostatic discharging current density from 0 to 0.75 mA cm^{-2}. The voltage was monitored for 60 s at each current density, with 20 s of rest before the next measurement on the same device. Long-time galvanostatic discharge was carried out continuously until the voltage dropped below zero for more than 1 min, when the battery was considered dead. Deionized water (4 to 8 μl) was added to compensate for the evaporation of water from the electrolyte droplet if the discharge lasted longer than 2000 s.

Short circuit discharge experiment

The bottle containing short-circuited picoliter batteries was agitated, and 10 μl of dispersion was drop-casted onto a glass slide. After drying, a hydrophobic PMMA well was pipetted around the batteries by hand. The batteries on slides were observed continuously under a Zeiss microscope (50× objective) after adding 100 μl of the PBS electrolyte until the batteries were fully discharged. The PBS electrolyte was bubbled with pure oxygen for 5 min to create an oxygen-saturated solution. When using this solution, a rubber well and a thin glass cover slide were used to seal the volume, preventing gas exchange with ambient air. The oxygen level was measured with an RCYAGO dissolved oxygen meter.

Memristor switching experiment

The batteries for powering the memristor, the actuator, the oscillator, and the sensors were all on the substrate. Picoliter batteries with wires (Fig. 2A) and memristors were connected to probe needles, and the needles were then connected through external cables. The initial resistance of memristors was recorded using a semiconductor analyzer. After disconnecting the cables from the semiconductor analyzer, we added 12.5 μl of the PBS electrolyte to the battery. The memristors were disconnected from the batteries 20 min later, and the final resistance was recorded. For the control devices, we measured the resistance of a device at rest in the off state every 20 min.

Actuator experiment

Pt-Ti bimorph actuators were fabricated on a Cu sacrificial layer according to the procedure reported previously (*9*). They were released by etching away Cu substrate in an ammonium persulfate solution (4 mg ml^{-1}) overnight. The floating actuators were then transferred with the Si wafer into a petri dish with PBS solution. Individual actuators were picked up by parylene-coated Ir/Pt probes (Microprobes for Life Science). The actuators were first tested with 0.4-V amplitude cyclic voltammetry at a sweep rate of 73 mV s^{-1}, with a Pt wire as the counter and reference electrode. Then, the actuator was connected to a picoliter battery in a separate solution with external wires. The polarity of connection was switched to cause cycles of actuation by manually reconnecting wires at a regular pace until the battery fully discharged and the actuation stopped. The state of the actuator was filmed in the meantime. For the recording of current, a semiconductor parameter analyzer was connected in series with the battery and set to maintain a constant voltage of 0 V.

Sensor experiment

Picoliter batteries with wires and chemical sensors were connected to probe needles, and the needles were then connected through external cables. Before starting the program, 12.5 μl of the PBS electrolyte was added to the battery. For the recording of current, a semiconductor parameter analyzer was connected in series with the battery and set to maintain a constant voltage of 0 V. The chemical sensors were initially dry; after being powered for a few minutes, a 1.5-μl droplet containing the analyte TEA was added to the sensor.

Oscillator experiment

One picoliter battery with wires was connected to a resistor, a capacitor, and two inverters through probe needles and cables according to the circuit in Fig. 6C. Before starting the program, 12.5 μl of the PBS electrolyte was added to the battery. The current was recorded until the battery ran out of charge.

Statistical analysis

Figures and tables present data from individual experiments without the application of statistical methods unless noted otherwise. All data are reported as either the mean or the mean ± SE unless specified differently. The discharge rate analysis, demonstrated in fig. S24 and Supplementary Discussion, was conducted using a nonlinear least squares method in MATLAB.

Supplementary Materials

The PDF file includes:
Figs. S1 to S30
Tables S1 to S3
Discussion and Method
References (*91–108*)

Other Supplementary Material for this manuscript includes the following:
Movies S1 to S3

REFERENCES AND NOTES

1. J. M. Kahn, R. H. Katz, K. S. J. Pister, Next century challenges: Mobile networking for 'smart dust', in *Proceedings of the 5th Annual ACM/IEEE International Conference on Mobile Computing and Networking* (ACM, 1999), pp. 271–278.
2. B. A. Warneke, K. S. J. Pister, An ultra-low energy microcontroller for smart dust wireless sensor networks, in *2004 IEEE International Solid-State Circuits Conference (IEEE Cat. No.04CH37519)* (IEEE, 2004), pp. 316–317.
3. M. Fojtik, D. Kim, G. Chen, Y.-S. Lin, D. Fick, J. Park, M. Seok, M.-T. Chen, Z. Foo, D. Blaauw, D. Sylvester, A millimeter-scale energy-autonomous sensor system with stacked battery and solar cells. *IEEE J. Solid-State Circuits* **48**, 801–813 (2013).
4. X. Wu, I. Lee, Q. Dong, K. Yang, D. Kim, J. Wang, Y. Peng, Y. Zhang, M. Saligane, M. Yasuda, K. Kumeno, F. Ohno, S. Miyoshi, M. Kawaminami, D. Sylvester, D. Blaauw, A 0.04MM^{3}16NW wireless and batteryless sensor system with integrated cortex-M0+ processor and optical communication for cellular temperature measurement, in *2018 IEEE Symposium on VLSI Circuits* (IEEE, 2018), pp. 191–192.
5. Y. Chen, H. Wang, E. F. Helbling, N. T. Jafferis, R. Zufferey, A. Ong, K. Ma, N. Gravish, P. Chirarattananon, M. Kovac, R. J. Wood, A biologically inspired, flapping-wing, hybrid aerial-aquatic microrobot. *Sci. Robot.* **2**, eaao5619 (2017).
6. X. Yang, L. Chang, N. O. Pérez-Arancibia, An 88-milligram insect-scale autonomous crawling robot driven by a catalytic artificial muscle. *Sci. Robot.* **5**, eaba0015 (2020).
7. A. M. Brooks, M. S. Strano, A conceptual advance that gives microrobots legs. *Nature* **584**, 530–531 (2020).
8. A. J. Cortese, C. L. Smart, T. Wang, M. F. Reynolds, S. L. Norris, Y. Ji, S. Lee, A. Mok, C. Wu, F. Xia, N. I. Ellis, A. C. Molnar, C. Xu, P. L. McEuen, Microscopic sensors using optical wireless integrated circuits. *Proc. Natl. Acad. Sci. U.S.A.* **117**, 9173–9179 (2020).
9. M. Z. Miskin, A. J. Cortese, K. Dorsey, E. P. Esposito, M. F. Reynolds, Q. Liu, M. Cao, D. A. Muller, P. L. McEuen, I. Cohen, Electronically integrated, mass-manufactured, microscopic robots. *Nature* **584**, 557–561 (2020).
10. V. B. Koman, P. Liu, D. Kozawa, A. T. Liu, A. L. Cottrill, Y. Son, J. A. Lebron, M. S. Strano, Colloidal nanoelectronic state machines based on 2D materials for aerosolizable electronics. *Nat. Nanotechnol.* **13**, 819–827 (2018).
11. P. Liu, A. T. Liu, D. Kozawa, J. Dong, J. F. Yang, V. B. Koman, M. Saccone, S. Wang, Y. Son, M. H. Wong, M. S. Strano, Autoperforation of 2D materials for generating two-terminal memristive Janus particles. *Nat. Mater.* **17**, 1005–1012 (2018).
12. A. T. Liu, J. F. Yang, L. N. LeMar, G. Zhang, A. Pervan, T. D. Murphey, M. S. Strano, Autoperforation of two-dimensional materials to generate colloidal state machines capable of locomotion. *Faraday Discuss.* **227**, 213–232 (2021).
13. A. T. Liu, M. Hempel, J. F. Yang, A. M. Brooks, A. Pervan, V. B. Koman, G. Zhang, D. Kozawa, S. Yang, D. I. Goldman, M. Z. Miskin, A. W. Richa, D. Randall, T. D. Murphey, T. Palacios, M. S. Strano, Colloidal robotics. *Nat. Mater.* **22**, 1453–1462 (2023).
14. M. Zhu, O. G. Schmidt, Tiny robots and sensors need tiny batteries—Here's how to do it. *Nature* **589**, 195–197 (2021).
15. H. Tang, D. D. Karnaushenko, V. Neu, F. Gabler, S. Wang, L. Liu, Y. Li, J. Wang, M. Zhu, O. G. Schmidt, Stress-actuated spiral microelectrode for high-performance lithium-ion microbatteries. *Small* **16**, e2002410 (2020).
16. K. Sun, T. Wei, B. Y. Ahn, J. Y. Seo, S. J. Dillon, J. A. Lewis, 3D printing of interdigitated Li-ion microbattery architectures. *Adv. Mater.* **25**, 4539–4543 (2013).
17. J. H. Pikul, H. Gang Zhang, J. Cho, P. V. Braun, W. P. King, High-power lithium ion microbatteries from interdigitated three-dimensional bicontinuous nanoporous electrodes. *Nat. Commun.* **4**, 1732 (2013).
18. W. Lai, C. K. Erdonmez, T. F. Marinis, C. K. Bjune, N. J. Dudney, F. Xu, R. Wartena, Y. Chiang, Ultrahigh-energy-density microbatteries enabled by new electrode architecture and micropackaging design. *Adv. Mater.* **22**, E139–E144 (2010).
19. B. Jia, C. Zhang, M. Liu, Z. Li, J. Wang, L. Zhong, C. Han, M. Qin, X. Huang, Integration of microbattery with thin-film electronics for constructing an integrated transparent microsystem based on InGaZnO. *Nat. Commun.* **14**, 5330 (2023).
20. S. Kim, A. Patra, R. R. Kohlmeyer, S. Jo, X. Yue, A. Johnson, C. T. Kiggins, B. Zahiri, K. Jeong, J. Koo, T. Kang, P. Sun, J. B. Cook, J. H. Pikul, P. V. Braun, Serially integrated high-voltage and high power miniature batteries. *Cell Rep. Phys. Sci.* **4**, 101205 (2023).
21. L. Liu, Q. Weng, X. Lu, X. Sun, L. Zhang, O. G. Schmidt, Advances on microsized on-chip lithium-ion batteries. *Small* **13**, 1701847 (2017).
22. Y. Lee, V. K. Bandari, Z. Li, M. Medina-Sánchez, M. F. Maitz, D. Karnaushenko, M. V. Tsurkan, D. D. Karnaushenko, O. G. Schmidt, Nano-biosupercapacitors enable autarkic sensor operation in blood. *Nat. Commun.* **12**, 4967 (2021).
23. Y. Li, M. Zhu, V. K. Bandari, D. D. Karnaushenko, D. Karnaushenko, F. Zhu, O. G. Schmidt, On-chip batteries for dust-sized computers. *Adv. Energy Mater.* **12**, 2103641 (2022).
24. Z. Qu, M. Zhu, Y. Yin, Y. Huang, H. Tang, J. Ge, Y. Li, D. D. Karnaushenko, D. Karnaushenko, O. G. Schmidt, A sub-square-millimeter microbattery with milliampere-hour-level footprint capacity. *Adv. Energy Mater.* **12**, 2200714 (2022).
25. A. S. Teran, J. Wong, W. Lim, G. Kim, Y. Lee, D. Blaauw, J. D. Phillips, AlGaAs photovoltaics for indoor energy harvesting in mm-scale wireless sensor nodes. *IEEE Trans. Electron. Devices* **62**, 2170–2175 (2015).
26. D. A. Funke, P. Mayr, T. Maeke, J. S. McCaskill, A. Sharma, L. Straczek, J. Oehm, Ultra low-power, -area and -frequency CMOS thyristor based oscillator for autonomous microsystems. *Analog Integr. Circuits Signal Process.* **89**, 347–356 (2016).
27. F. Maksimovic, B. Wheeler, D. C. Burnett, O. Khan, S. Mesri, I. Suciu, L. Lee, A. Moreno, A. Sundararajan, B. Zhou, R. Zoll, A. Ng, T. Chang, X. Villajosana, T. Watteyne, A. Niknejad, K. S. J. Pister, A crystal-free single-chip micro mote with integrated 802.15.4 compatible transceiver, sub-mW BLE compatible beacon transmitter, and cortex M0, in *2019 Symposium on VLSI Circuits* (IEEE, 2019), pp. C88–C89.
28. O. Aiello, P. Crovetti, M. Alioto, A sub-leakage PW-power HZ-range relaxation oscillator operating with 0.3V-1.8V unregulated supply, in *2018 IEEE Symposium on VLSI Circuits* (IEEE, 2018), pp. 119–120.
29. M. Hempel, V. Schroeder, C. Park, V. B. Koman, M. Xue, E. McVay, S. Spector, M. Dubey, M. S. Strano, J. Park, J. Kong, T. Palacios, SynCells: A 60 × 60 μm^2 electronic platform with remote actuation for sensing applications in constrained environments. *ACS Nano* **15**, 8803–8812 (2021).
30. M. Zhu, O. G. Schmidt, Batteries for small-scale robotics. *MRS Bull.* **49**, 115–124 (2024).
31. N. Masurkar, G. Babu, S. Porchelvan, L. M. Reddy Arava, Millimeter-scale lithium ion battery packaging for high-temperature sensing applications. *J. Power Sources* **399**, 179–185 (2018).
32. S. Ferrari, M. Loveridge, S. D. Beattie, M. Jahn, R. J. Dashwood, R. Bhagat, Latest advances in the manufacturing of 3D rechargeable lithium microbatteries. *J. Power Sources* **286**, 25–46 (2015).
33. S. Zheng, X. Shi, P. Das, Z. Wu, X. Bao, The road towards planar microbatteries and micro-supercapacitors: From 2D to 3D device geometries. *Adv. Mater.* **31**, e1900583 (2019).
34. J. F. M. Oudenhoven, L. Baggetto, P. H. L. Notten, All-solid-state lithium-ion microbatteries: A review of various three-dimensional concepts. *Adv. Energy Mater.* **1**, 10–33 (2011).
35. D. Cao, Y. Xing, K. Tantratian, X. Wang, Y. Ma, A. Mukhopadhyay, Z. Cheng, Q. Zhang, Y. Jiao, L. Chen, H. Zhu, 3D printed high-performance lithium metal microbatteries enabled by nanocellulose. *Adv. Mater.* **31**, e1807313 (2019).
36. M. M. Shaijumon, E. Perre, B. Daffos, P. Taberna, J. Tarascon, P. Simon, Nanoarchitectured 3D cathodes for Li-ion microbatteries. *Adv. Mater.* **22**, 4978–4981 (2010).
37. M. Létiche, E. Eustache, J. Freixas, A. Demortière, V. De Andrade, L. Morgenroth, P. Tilmant, F. Vaurette, D. Troadec, P. Roussel, T. Brousse, C. Lethien, Atomic layer deposition of functional layers for on chip 3D Li-ion all solid state microbattery. *Adv. Energy Mater.* **7**, 1601402 (2017).
38. P. Sun, X. Li, J. Shao, P. V. Braun, High-performance packaged 3D Lithium-ion microbatteries fabricated using imprint lithography. *Adv. Mater.* **33**, 2006229 (2021).
39. Y. Wang, S. Cartmell, Q. Li, J. Xiao, H. Li, Z. D. Deng, J.-G. Zhang, A reliable sealing method for microbatteries. *J. Power Sources* **341**, 443–447 (2017).
40. Y. Zhou, X. Jia, D. Pang, S. Jiang, M. Zhu, G. Lu, Y. Tian, C. Wang, D. Chao, G. Wallace, An integrated Mg battery-powered iontophoresis patch for efficient and controllable transdermal drug delivery. *Nat. Commun.* **14**, 297 (2023).
41. Y. Su, J. Falgenhauer, A. Polity, T. Leichtweiß, A. Kronenberger, J. Obel, S. Zhou, D. Schlettwein, J. Janek, B. K. Meyer, LiPON thin films with high nitrogen content for application in lithium batteries and electrochromic devices prepared by RF magnetron sputtering. *Solid State Ion.* **282**, 63–69 (2015).
42. F. Le Cras, B. Pecquenard, V. Dubois, V. Phan, D. Guy-Bouyssou, All-solid-state lithium-ion microbatteries using silicon nanofilm anodes: High performance and memory effect. *Adv. Energy Mater.* **5**, 1501061 (2015).
43. H. Lhermet, C. Condemine, M. Plissonnier, R. Salot, P. Audebert, M. Rosset, Efficient power management circuit: From thermal energy harvesting to above-IC microbattery energy storage. *IEEE J. Solid-State Circuits* **43**, 246–255 (2008).
44. S. Oukassi, R. Salot, A. Bazin, C. Secouard, I. Chevalier, S. Poncet, S. Poulet, J.-M. Boissel, F. Geffraye, J. Brun, Millimeter scale thin film batteries for integrated high energy density storage, in *2019 IEEE International Electron Devices Meeting (IEDM)* (IEEE, 2019), pp. 26.1.1–26.1.4.
45. J. Fu, Z. P. Cano, M. G. Park, A. Yu, M. Fowler, Z. Chen, Electrically rechargeable zinc–air batteries: Progress, challenges, and perspectives. *Adv. Mater.* **29**, 1604685 (2017).

46. Y. Li, H. Dai, Recent advances in zinc–air batteries. *Chem. Soc. Rev.* **43**, 5257–5275 (2014).
47. J. Zhang, Q. Zhou, Y. Tang, L. Zhang, Y. Li, Zinc–air batteries: Are they ready for prime time? *Chem. Sci.* **10**, 8924–8929 (2019).
48. S. R. Meskon, R. Othman, M. H. Ani, A secondary, coplanar design Ni/MCM-41/Zn microbattery. *IOP Conf. Ser. Mater. Sci. Eng.* **290**, 012073 (2018).
49. M. Liu, X. Pu, Z. Cong, Z. Liu, T. Liu, Y. Chen, J. Fu, W. Hu, Z. L. Wang, Resist-dyed textile alkaline Zn microbatteries with significantly suppressed Zn dendrite growth. *ACS Appl. Mater. Interfaces* **11**, 5095–5106 (2019).
50. Z. Hao, L. Xu, Q. Liu, W. Yang, X. Liao, J. Meng, X. Hong, L. He, L. Mai, On-chip Ni–Zn microbattery based on hierarchical ordered porous Ni@Ni(OH)$_2$ microelectrode with ultrafast ion and electron transport kinetics. *Adv. Funct. Mater.* **29**, 1808470 (2019).
51. P. H. Humble, J. N. Harb, Optimization of nickel-zinc microbatteries for hybrid powered microsensor systems. *J. Electrochem. Soc.* **150**, A1182 (2003).
52. R. Trócoli, A. Morata, M. Fehse, M. Stchakovsky, A. Sepúlveda, A. Tarancón, High specific power dual-metal-ion rechargeable microbatteries based on LiMn$_2$O$_4$ and zinc for miniaturized applications. *ACS Appl. Mater. Interfaces* **9**, 32713–32719 (2017).
53. C. C. Ho, J. W. Evans, P. K. Wright, Direct write dispenser printing of a zinc microbattery with an ionic liquid gel electrolyte. *J. Micromech. Microeng.* **20**, 104009 (2010).
54. B. He, Q. Zhang, L. Li, J. Sun, P. Man, Z. Zhou, Q. Li, J. Guo, L. Xie, C. Li, X. Wang, J. Zhao, T. Zhang, Y. Yao, High-performance flexible all-solid-state aqueous rechargeable Zn–MnO$_2$ microbatteries integrated with wearable pressure sensors. *J. Mater. Chem. A* **6**, 14594–14601 (2018).
55. G. Sun, X. Jin, H. Yang, J. Gao, L. Qu, An aqueous Zn–MnO$_2$ rechargeable microbattery. *J. Mater. Chem. A* **6**, 10926–10931 (2018).
56. X. Wang, S. Zheng, F. Zhou, J. Qin, X. Shi, S. Wang, C. Sun, X. Bao, Z.-S. Wu, Scalable fabrication of printed Zn//MnO2 planar micro-batteries with high volumetric energy density and exceptional safety. *Natl. Sci. Rev.* **7**, 64–72 (2020).
57. M. Zhu, J. Hu, Q. Lu, H. Dong, D. D. Karnaushenko, C. Becker, D. Karnaushenko, Y. Li, H. Tang, Z. Qu, J. Ge, O. G. Schmidt, A patternable and in situ formed polymeric zinc blanket for a reversible zinc anode in a skin-mountable microbattery. *Adv. Mater.* **33**, 2007497 (2021).
58. C. B. Arnold, H. Kim, A. Piqué, Laser direct write of planar alkaline microbatteries. *Appl. Phys. A* **79**, 417–420 (2004).
59. C. C. Ho, K. Murata, D. A. Steingart, J. W. Evans, P. K. Wright, A super ink jet printed zinc–silver 3D microbattery. *J. Micromech. Microeng.* **19**, 094013 (2009).
60. J. Shi, S. Wang, X. Chen, Z. Chen, X. Du, T. Ni, Q. Wang, L. Ruan, W. Zeng, Z. Huang, An ultrahigh energy density quasi-solid-state zinc ion microbattery with excellent flexibility and thermostability. *Adv. Energy Mater.* **9**, 1901957 (2019).
61. Z. Qu, J. Ma, Y. Huang, T. Li, H. Tang, X. Wang, S. Liu, K. Zhang, J. Lu, D. D. Karnaushenko, D. Karnaushenko, M. Zhu, O. G. Schmidt, A photolithographable electrolyte for deeply rechargeable zn microbatteries in on-chip devices. *Adv. Mater.* **36**, 2310667 (2024).
62. H. Saputra, R. Othman, M. H. Ani, A. G. E. Sutjipto, R. Muhida, High energy density zinc–air microbattery utilising inorganic MCM-41 membrane. *Mater. Res. Innov.* **15**, s114–s117 (2011).
63. M. Synodis, J. Pikul, S. A. B. Allen, M. G. Allen, Vertically integrated high voltage Zn-air batteries enabled by stacked multilayer electrodeposition. *J. Power Sources* **449**, 227566 (2020).
64. P. Nadeau, D. El-Damak, D. Glettig, Y. L. Kong, S. Mo, C. Cleveland, L. Booth, N. Roxhed, R. Langer, A. P. Chandrakasan, G. Traverso, Prolonged energy harvesting for ingestible devices. *Nat. Biomed. Eng.* **1**, 0022 (2017).
65. L. Yin, X. Huang, H. Xu, Y. Zhang, J. Lam, J. Cheng, J. A. Rogers, Materials, designs, and operational characteristics for fully biodegradable primary batteries. *Adv. Mater.* **26**, 3879–3884 (2014).
66. F. Chamran, Hong-Seok Min, B. Dunn, Chang-Jin Kim, Zinc-air microbattery with electrode array of zinc microposts, in *2007 IEEE 20th International Conference on Micro Electro Mechanical Systems (MEMS)* (IEEE, 2007), pp. 871–874.
67. M. Synodis, J. Pikul, S. A. B. Allen, M. Allen, Integrated fabrication of serially connected high voltage microbatteries via multilayer electrodeposition, in *2019 20th International Conference on Solid-State Sensors, Actuators and Microsystems & Eurosensors XXXIII (TRANSDUCERS & EUROSENSORS XXXIII)* (IEEE, 2019), pp. 789–792.
68. K. B. Lee, L. Lin, Electrolyte-based on-demand and disposable microbattery. *J. Microelectromech. Syst.* **12**, 840–847 (2003).
69. A. Armutlulu, Y. Fang, S.-H. Kim, C.-H. Ji, S. A. B. Allen, M. G. Allen, High-current zinc-air microbattery based on a micromachined multilayer lateral metallic scaffold, in *Proceedings of PowerMEMS* (IEEE, 2010), pp. 107–110.
70. A. Armutlulu, Y. Fang, S. H. Kim, C. H. Ji, S. A. Bidstrup Allen, M. G. Allen, A MEMS-enabled 3D zinc–air microbattery with improved discharge characteristics based on a multilayer metallic substructure. *J. Micromech. Microeng.* **21**, 104011 (2011).
71. H. Jimbo, N. Miki, Gastric-fluid-utilizing micro battery for micro medical devices. *Sens. Actuators B Chem.* **134**, 219–224 (2008).
72. H. Zhang, Z. Qu, H. Tang, X. Wang, R. Koehler, M. Yu, C. Gerhard, Y. Yin, M. Zhu, K. Zhang, O. G. Schmidt, On-chip integration of a covalent organic framework-based catalyst into a miniaturized zn–air battery with high energy density. *ACS Energy Lett.* **6**, 2491–2498 (2021).
73. A. J. Bandodkar, S. P. Lee, I. Huang, W. Li, S. Wang, C.-J. Su, W. J. Jeang, T. Hang, S. Mehta, N. Nyberg, P. Gutruf, J. Choi, J. Koo, J. T. Reeder, R. Tseng, R. Ghaffari, J. A. Rogers, Sweat-activated biocompatible batteries for epidermal electronic and microfluidic systems. *Nat. Electron.* **3**, 554–562 (2020).
74. E. F. Garay, R. Bashirullah, Biofluid activated microbattery for disposable microsystems. *J. Microelectromechanical Syst.* **24**, 70–79 (2015).
75. W. Shin, J. Lee, Y. Kim, H. Steinfink, A. Heller, Ionic conduction in Zn$_3$ (PO$_4$)$_2$·4H$_2$O enables efficient discharge of the zinc anode in serum. *J. Am. Chem. Soc.* **127**, 14590–14591 (2005).
76. Y. F. Zheng, X. N. Gu, F. Witte, Biodegradable metals. *Mater. Sci. Eng. R: Rep.* **77**, 1–34 (2014).
77. M. Tsang, A. Armutlulu, A. W. Martinez, S. A. B. Allen, M. G. Allen, Biodegradable magnesium/iron batteries with polycaprolactone encapsulation: A microfabricated power source for transient implantable devices. *Microsyst. Nanoeng.* **1**, 15024 (2015).
78. R. M. Souto, Y. González-García, A. C. Bastos, A. M. Simões, Investigating corrosion processes in the micrometric range: A SVET study of the galvanic corrosion of zinc coupled with iron. *Corros. Sci.* **49**, 4568–4580 (2007).
79. J. Li, H.-M. Yin, X.-B. Li, E. Okunishi, Y.-L. Shen, J. He, Z.-K. Tang, W.-X. Wang, E. Yücelen, C. Li, Y. Gong, L. Gu, S. Miao, L.-M. Liu, J. Luo, Y. Ding, Surface evolution of a Pt–Pd–Au electrocatalyst for stable oxygen reduction. *Nat. Energy* **2**, 17111 (2017).
80. X. Tian, X. Zhao, Y.-Q. Su, L. Wang, H. Wang, D. Dang, B. Chi, H. Liu, E. J. M. Hensen, X. W. Lou, B. Y. Xia, Engineering bunched Pt-Ni alloy nanocages for efficient oxygen reduction in practical fuel cells. *Science* **366**, 850–856 (2019).
81. L. Cao, G. Fang, H. Cao, X. Duan, Photopatterning and electrochemical energy storage properties of an on-chip organic radical microbattery. *Langmuir* **35**, 16079–16086 (2019).
82. J. I. Hur, L. C. Smith, B. Dunn, High areal energy density 3D lithium-ion microbatteries. *Joule* **2**, 1187–1201 (2018).
83. Q. Liu, G. Zhang, N. Chen, X. Feng, C. Wang, J. Wang, X. Jin, L. Qu, The first flexible dual-ion microbattery demonstrates superior capacity and ultrahigh energy density: Small and powerful. *Adv. Funct. Mater.* **30**, 2002086 (2020).
84. J. F. Yang, A. T. Liu, T. A. Berrueta, G. Zhang, A. M. Brooks, V. B. Koman, S. Yang, X. Gong, T. D. Murphey, M. S. Strano, Memristor circuits for colloidal robotics: Temporal access to memory, sensing, and actuation. *Adv. Intell. Syst.* **4**, 2100205 (2022).
85. Q. Liu, W. Wang, M. F. Reynolds, M. C. Cao, M. Z. Miskin, T. A. Arias, D. A. Muller, P. L. McEuen, I. Cohen, Micrometer-sized electrically programmable shape-memory actuators for low-power microrobotics. *Sci. Robot.* **6**, 6663 (2021).
86. A. C. Molnar, S. Lee, A. Cortese, P. McEuen, S. Sadeghi, S. Ghajari, Nanoliter-scale autonomous electronics: Advances, challenges, and opportunities, in *2021 IEEE Custom Integrated Circuits Conference (CICC)* (IEEE, 2021), pp. 1–6.
87. M. Wang, D. Vecchio, C. Wang, A. Emre, X. Xiao, Z. Jiang, P. Bogdan, Y. Huang, N. A. Kotov, Biomorphic structural batteries for robotics. *Sci. Robot.* **5**, eaba1912 (2020).
88. C. A. Aubin, B. Gorissen, E. Milana, P. R. Buskohl, N. Lazarus, G. A. Slipher, C. Keplinger, J. Bongard, F. Iida, J. A. Lewis, R. F. Shepherd, Towards enduring autonomous robots via embodied energy. *Nature* **602**, 393–402 (2022).
89. J. H. Pikul, J. Liu, P. V. Braun, W. P. King, Integration of high capacity materials into interdigitated mesostructured electrodes for high energy and high power density primary microbatteries. *J. Power Sources* **315**, 308–315 (2016).
90. S. K. Sailapu, A. Blanquer, M. Duch, J. P. Esquivel, C. Nogués, J. Esteve, N. Sabaté, Self-activated microbatteries to promote cell death through local electrical stimulation. *Nano Energy* **83**, 105852 (2021).
91. Panasonic, Specifications for NCR18650GA; https://orbtronic.com/content/Datasheet-specs-Sanyo-Panasonic-NCR18650GA-3500mah.pdf.
92. M. E. McMahon, R. J. Santucci, J. R. Scully, Advanced chemical stability diagrams to predict the formation of complex zinc compounds in a chloride environment. *RSC Adv.* **9**, 19905–19916 (2019).
93. H. Klumbies, L. Müller-Meskamp, T. Mönch, S. Schubert, K. Leo, The influence of laterally inhomogeneous corrosion on electrical and optical calcium moisture barrier characterization. *Rev. Sci. Instrum.* **84**, 024103 (2013).
94. A. M. Simões, A. C. Bastos, M. G. Ferreira, Y. González-García, S. González, R. M. Souto, Use of SVET and SECM to study the galvanic corrosion of an iron–zinc cell. *Corros. Sci.* **49**, 726–739 (2007).
95. D.-L. Zhang, W. Wang, Y. Li, An electrode array study of electrochemical inhomogeneity of zinc in zinc/steel couple during galvanic corrosion. *Corros. Sci.* **52**, 1277–1284 (2010).
96. H. Wang, P. P. Mercier, A reference-free capacitive-discharging oscillator architecture consuming 44.4 pW/75.6 nW at 2.8 Hz/6.4 kHz. *IEEE J. Solid-State Circuits* **51**, 1423–1435 (2016).

97. Y.-S. Lin, D. Sylvester, D. Blaauw, A sub-pW timer using gate leakage for ultra low-power sub-Hz monitoring systems, in *2007 IEEE Custom Integrated Circuits Conference* (IEEE, 2007), pp. 397–400.
98. Y.-H. Lee, S.-Y. Peng, C.-C. Chiu, A. C.-H. Wu, K.-H. Chen, Y.-H. Lin, S.-W. Wang, T.-Y. Tsai, C.-C. Huang, C.-C. Lee, A low quiescent current asynchronous digital-LDO with PLL-modulated fast-DVS power management in 40 nm SoC for MIPS performance improvement. *IEEE J. Solid-State Circuits* **48**, 1018–1030 (2013).
99. P. P. Mercier, A. C. Lysaght, S. Bandyopadhyay, A. P. Chandrakasan, K. M. Stankovic, Energy extraction from the biologic battery in the inner ear. *Nat. Biotechnol.* **30**, 1240–1243 (2012).
100. D. A. Funke, P. Mayr, L. Straczek, J. S. McCaskill, J. Oehm, N. Pohl, A 200 μm by 100 μm smart dust system with an average current consumption of 1.3 nA, in *2016 IEEE International Conference on Electronics, Circuits and Systems (ICECS)* (IEEE, 2016), pp. 512–515.
101. J. Choi, E. Aklimi, C. Shi, D. Tsai, H. Krishnaswamy, K. L. Shepard, Matching the power, voltage, and size of biological systems: A nW-scale, 0.023-mm^3 pulsed 33-GHz radio transmitter operating from a 5 kT/q-supply voltage. *IEEE Trans. Circuits Syst. I: Regul. Pap.* **62**, 1950–1958 (2015).
102. M. H. Ghaed, G. Chen, R. Haque, M. Wieckowski, Y. Kim, G. Kim, Y. Lee, I. Lee, D. Fick, D. Kim, M. Seok, K. D. Wise, D. Blaauw, D. Sylvester, Circuits for a cubic-millimeter energy-autonomous wireless intraocular pressure monitor. *IEEE Trans. Circuits Syst. I: Regul. Pap.* **60**, 3152–3162 (2013).
103. Y. Lee, S. Bang, I. Lee, Y. Kim, G. Kim, M. H. Ghaed, P. Pannuto, P. Dutta, D. Sylvester, D. Blaauw, A modular 1 mm^3 die-stacked sensing platform with low power I^{2}C inter-die communication and multi-modal energy harvesting. *IEEE J. Solid-State Circuits* **48**, 229–243 (2013).
104. S. O'Driscoll, S. Korhummel, P. Cong, Y. Zou, K. Sankaragomathi, J. Zhu, T. Deyle, A. Dastgheib, B. Lu, M. Tierney, J. Shao, C. Gutierrez, S. Jones, H. Yao, A 200μm × 200μm × 100μm, 63nW, 2.4GHz injectable fully-monolithic wireless bio-sensing system, in *2017 IEEE Radio Frequency Integrated Circuits Symposium* (*RFIC*) (IEEE, 2017), pp. 256–259.
105. S. Lee, A. J. Cortese, P. Trexel, E. R. Agger, P. L. McEuen, A. C. Molnar, A 330μm×90μm opto-electronically integrated wireless system-on-chip for recording of neural activities, in *2018 IEEE International Solid - State Circuits Conference* - (*ISSCC*) (IEEE, 2018), pp. 292–294.
106. J. Lim, E. Moon, M. Barrow, S. R. Nason, P. R. Patel, P. G. Patil, S. Oh, I. Lee, H.-S. Kim, D. Sylvester, D. Blaauw, C. A. Chestek, J. Phillips, T. Jang, 26.9 A 0.19×0.17mm^2 wireless neural recording IC for motor prediction with near-infrared-based power and data telemetry, in *2020 IEEE International Solid- State Circuits Conference* - (*ISSCC*) (IEEE, 2020), pp. 416–418.
107. S. Lee, A. J. Cortese, A. P. Gandhi, E. R. Agger, P. L. McEuen, A. C. Molnar, A 250 μm × 57 μm microscale opto-electronically transduced electrodes (MOTEs) for neural recording. *IEEE Trans. Biomed Circuits Syst.* **12**, 1256–1266 (2018).
108. Energizer, Energizer Zinc Air Prismatic Handbook; https://data.energizer.com/pdfs/zincairprismatichandbook.pdf.

Acknowledgments: Microfabrication for this work was performed at the Harvard University Center for Nanoscale Systems (CNS), a member of the National Nanotechnology Coordinated Infrastructure Network (NNCI), which is supported by the NSF under NSF award no. 1541959. G.Z. acknowledges support from the MathWorks Engineering Fellowship. We acknowledge the help provided by A. Penn at MIT.nano with collecting EDS data. **Funding:** We are appreciative of funding from the US Army Research Office MURI grant on Formal Foundations of Algorithmic Matter and Emergent Computation (award no. W911NF-19-1-0233) for the metrological and computational tools used in this work. System fabrication and particulate engineering were supported using funds from the US Department of Energy (DOE), Office of Science, Basic Energy Sciences (grant DE-FG02-08ER46488). **Author contributions:** G.Z. conceived the idea and designed the picoliter batteries. G.Z. and S.Y. fabricated and characterized the picoliter batteries. D.G.-M. and M.Z.M. provided the actuators. Y.Z. performed XRD measurement. V.B.K. and J.F.Y. assisted with the cleanroom fabrication and writing. M.K. helped with STEM analysis, preparation of SWNT sensors, and thermal evaporation. S.X.L. designed the sacrificial layer. A.T.L. assisted with characterization of the probe station. J.F.Y., S.Y., and A.M.B. performed part of the actuator characterization. S.Y. performed micro–inkjet printing of ionic liquid electrolyte. G.Z., S.Y., and M.S.S. cowrote the manuscript. All authors contributed to discussions. **Competing interests:** The authors declare that they have no competing interests. **Data and materials availability:** All data needed to support the conclusions of this manuscript are included in the main text or Supplementary Materials. Data analysis and visualization code are available at DOI: 10.5281/zenodo.12720661.

Submitted 17 August 2022
Accepted 17 July 2024
Published 14 August 2024
10.1126/scirobotics.ade4642

Science Robotics

High energy density picoliter-scale zinc-air microbatteries for colloidal robotics

Ge Zhang, Sungyun Yang, Jing Fan Yang, David Gonzalez-Medrano, Marc Z. Miskin, Volodymyr B. Koman, Yuwen Zeng, Sylvia Xin Li, Matthias Kuehne, Albert Tianxiang Liu, Allan M. Brooks, Mahesh Kumar, and Michael S. Strano

Sci. Robot. **9** (93), eade4642. DOI: 10.1126/scirobotics.ade4642

Editor’s summary
Energy storage at the micrometer scale is an ever-growing challenge as robots are progressively downsized. Moreover, the use of wet chemistry in battery technologies limits their potential to be scaled down beyond millimeters in size. Zhang *et al*. have now developed a high energy density zinc-air battery at the picoliter scale in volume. Using photolithography, 10,000 batteries could be fabricated from a single 50.8-mm wafer and released into solution. Moreover, the batteries could achieve an energy density above 760 watt-hours per liter and were capable of powering micrometer-sized devices such as colloidal robots, sensors, and memristor circuits. —Amos Matsiko

Science Robotics (ISSN 2470-9476) is published by the American Association for the Advancement of Science. 1200 New York Avenue NW, Washington, DC 20005. The title *Science Robotics* is a registered trademark of AAAS.